ACS OMEGA

Open Access

This article is licensed under CC-BY-NC-ND 4.0

http://pubs.acs.org/journal/acsodf

Article

Preparation of a Porous Protein-Based Composite Material by In Situ Polymerization of Pickering High Internal Phase Emulsion for Adsorption of Lead Ions

Junzheng Wang, Maofeng Zhu, and Jierong Zhou*

Cite This: *ACS Omega* 2024, 9, 20142−20151

Read Online

ACCESS | Metrics & More | Article Recommendations

ABSTRACT: The preparation of complex porous materials using a small molecular surfactant as the stabilizer of a high internal phase emulsion can result in harm to the environment. In this study, porous composites based on soy protein isolate with poly(acrylic acid) were prepared by in situ polymerization of a high internal phase monomer emulsion with an internal phase volume fraction of 80%. The material was prepared from acrylic acid and an *N*,*N*-methyl diacrylic acid monomer solution as the continuous phase, peanut oil as the dispersed phase, and soy protein isolate as the composite stabilizer. Scanning electron microscopy showed that porous composites exhibited a concave/convex three-dimensional interpenetrating pore structure. Fourier-transform infrared spectra revealed the existence of many active groups such as carboxyl, amino, hydroxyl, and sulfhydryl. The composite had a high adsorption capacity for lead ions, even at low concentration, with a removal rate of up to 95.7%. The adsorption process conformed to a two-stage model involving internal diffusion and Langmuir isothermal adsorption. The maximum saturated adsorption capacity was 36.71 mg/g when the initial solution concentration was 150 mg/L, the adsorbent concentration was 7.0 g/L, and the adsorption mechanism involved chemical interactions between the lead ions and the composite groups −COOH, −OH, and −SH.

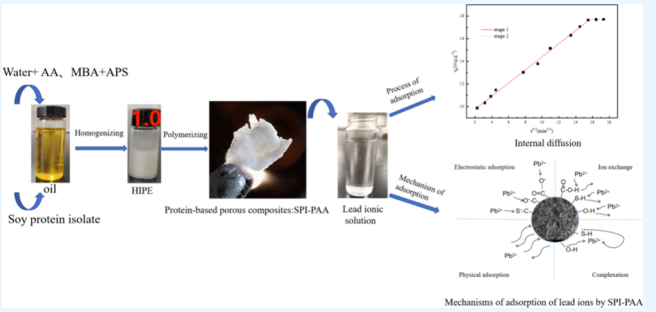

1. INTRODUCTION

Lead is a common toxic heavy metal pollutant in the environment that causes harm to both aquatic and terrestrial organisms and threatens human health and development through its bioaccumulation in food animals and crop plants.[1] At present, the main methods to control lead pollution include chemical precipitation, electrochemistry, ion exchange, membrane separation, and adsorption. Among these, the adsorption method is considered the most suitable treatment because of its simplicity and high efficiency.[2,3] Activated carbon, functionalized silica gel,[4] porous carbon nanofibers,[5] and biochar[6] have proven very effective at removing lead ions from the environment. As new adsorbent materials for the removal of heavy metals, porous composite materials have the advantages of excellent permeability, high porosity, adjustable pore size, and low density. The current techniques for preparing porous materials include the sol−gel method, gas-foaming method, phase separation method, and template method.[7−9]

The high internal phase emulsion (HIPE) template method has attracted much attention because of its ease of use, ability for modification of the synthesized HIPE polymers (polyHIPEs), high porosity, and large specific surface area. Success with the HIPE template method requires the choice of the proper stabilizer. Traditionally, HIPE stabilizers have been small molecule surfactants, such as CTAB,[10] Tween80,[11] Tween20,[12] Span80,[13] etc. However, these surfactants themselves are somewhat toxic and their removal requires a large amount of solvent for extraction, which limits their application in HIPE polymers. To stabilize HIPEs, researchers began testing solid inorganic nanoparticles made from nano-SiO_2,[14] TiO_2,[15] graphene oxide,[16] and Fe_3O_4;[17] however, the inorganic nanoparticles often required modification, which can be a cumbersome operation. Therefore, it is of great importance and value to develop solid nanoparticle stabilizers for HIPEs that are environmentally friendly, are easy to apply, and have strong emulsion stability and good biocompatibility as templates to prepare porous adsorbent polymer materials with open pore structures.

In recent years, protein-based particles, such as the new type of Pickering particle, have become popular in food processing. At present, there have been many reports of high internal

Received: January 5, 2024
Revised: April 6, 2024
Accepted: April 10, 2024
Published: April 25, 2024

ACS Publications

© 2024 The Authors. Published by American Chemical Society

phase Pickering emulsions stabilized with peanut protein, zein, wheat gliadin, and soy protein isolate (SPI) to replace trans-fatty acids, mayonnaise, and curcumin for embedding active substances.[18−26] However, there are few reports on the use of a high internal phase Pickering emulsion stabilized by SPI as a template for the preparation of porous polymer materials and the adsorption of heavy metal ions. Zhou et al.[20] prepared porous materials using alcohol-soluble wheat protein-chitosan composite particles as a stable HIPE template and investigated the adsorption capacity of corn oil. Yu[25] experimented with the preparation of porous materials using a wheat gliadin-stabilized HIPE template for the adsorption of Pb^{2+} and Cd^{2+} but did not investigate the adsorption mechanism.

In this study, SPI was used as the stabilizer, peanut oil as the dispersed phase, and acrylic acid (AA) and *N*,*N*-methylbis-(acrylic acid) (MBA) monomer solution as the continuous phases to prepare a HIPE with good stability and then use in situ polymerization with SPI to prepare protein-based porous materials to adsorb lead ions from solution. In this study, we examined the effects of factors such as oil phase volume fraction, SPI concentration, and temperature on the stability of HIPEs, measured the capacity for adsorption of lead ions on porous materials, and explored potential mechanisms. This study further expands upon the preparation methods of biocompatible and biodegradable porous polymer materials and the application of protein-based porous materials in wastewater treatment.

2. EXPERIMENTAL SECTION

2.1. Reagents and Instruments. All reagents were of analytical grade, and water was deionized. The following reagents were purchased from the indicated suppliers: acrylic acid (AA), Shanghai Aladdin Reagent Co., Ltd.; *N*,*N*-methylbis(acrylic acid) (MBA), Tianjin Comeo Chemical Reagent Co., Ltd.; soy protein isolate (SPI; purity, 98%), Shanghai McLean Biochemical Technology Co., Ltd.; ammonium persulfate (APS), *n*-hexane, lead nitrate, Xilong Scientific Co., Ltd.; peanut oil, Shandong Yuwang Bean Industry Co., Ltd.; *N*,*N*,*N*-tetramethylethylenediamine (TMEDA), Damao, Tianjin Chemical Reagent Factory.

The following instruments were obtained from the indicated suppliers: Spectrum-One Fourier transform infrared spectrometer (FTIR), PerkinElmer, USA; scanning electron microscope, JSM-7800F, Nippon Electronics Corporation; WFX-120B atomic absorption spectrophotometer, Beijing Beifang Rayleigh Analytical Instrument Co., Ltd.; Nikon 80i confocal fluorescence microscope, Shanghai Henghao Instrument Co., Ltd.; HH-2 digital display constant temperature water bath, Changzhou Aohua Instrument Co., Ltd.; THZ-C thermostatic oscillator, Taicang Experimental Equipment Factory; DZF-1 vacuum drying oven, Beijing Guangming Medical Instrument Co., Ltd.

2.2. Preparation of Protein-Based Porous Materials. Aqueous solutions of agglomerated soy protein isolate particles with different mass concentrations at different pH values were prepared and mixed with 3.0 g of AA and 0.3 g of MBA monomers. At the same time, 0.065 g of the initiator APS and 0.05 mg of the cross-linking agent TMEDA were added. The solution was stirred for 5 min, then peanut oil was added so that the volume fraction of the oil phase (internal phase) reached 80%, and the mixture was homogenized at 8000 rpm for 30 s to form the HIPE. The HIPEs were transferred to the molds, sealed, and polymerized in a water bath at 70 °C for 24 h to obtain a block polymer. The polymer was extracted with *n*-hexane in a Soxhlet apparatus for 24 h and vacuum-dried at 50 °C to constant weight to yield a protein-based porous material.

2.3. Structural Characterization and Performance Testing. The potassium bromide tableting method was used for FT-IR spectrometry of the samples over the wavenumber range of 4000 to 400 cm^{-1}. An electron microscope was used to image the micromorphology of the protein-based porous materials and perform X-ray photoelectron spectroscopy (XPS) analysis. The specific surface area of the sample was measured by using a specific surface area and pore size distribution meter. Confocal fluorescence microscopy of the HIPEs was used to characterize their microstructure, and the HIPEs were allowed to stand for a predetermined length of time while the stability of the material was visually observed. An atomic absorption spectrophotometer was used at a wavelength of 283 nm to determine the concentration of the lead ions in the solution.

2.4. Measurement of Adsorption of Lead Ions. For the adsorption determination, 20 mL of lead nitrate solution at a concentration of 150 mg/L was placed in a flask and incubated with 7.0 g/L protein-based porous composite at room temperature for 300 min with oscillation at a rate of 150 rpm. The concentration of lead ions in the filtered transparent liquid was measured, and the adsorption capacity and removal rate were calculated using eqs 1 and 2, respectively:

$$q_t = (C_0 - C_t) \times V/m \tag{1}$$

$$R = \frac{C_0 - C_t}{C_0} \times 100\% \tag{2}$$

where q_t is the adsorption capacity in mg/g, R is the removal rate as a percentage of the initial concentration, C_0 and C_t are the lead ion concentrations in mg/L before and after adsorption, respectively, V is the volume of the lead ion solution in mL, and m is the mass of the adsorbent in mg.

To determine the adsorption kinetics, we tested the fit of the adsorption data to a pseudo-first-order kinetic model, a pseudo-second-order kinetic model, and an internal diffusion model (eqs 3−5):[27,28]

$$q_t = q_e(1 - e^{-k_1 t}) \tag{3}$$

$$q_t = \frac{k_2 q_e^2 t}{1 + k_2 q_e^1} \tag{4}$$

$$q_t = K_i t^{1/2} + C \tag{5}$$

where q_t and q_e are the amount of adsorbed lead ions and the equilibrium adsorption amount at time t in mg/g, respectively, k_1 is the pseudo-first-order adsorption rate constant (/min), k_2 is the pseudo-second-order adsorption rate constant (g/(mg·min)), and K_i is the internal diffusion coefficient (g/(mg·min)).

The isothermal adsorption experiment used the Langmuir model and Freundlich model (eqs 6 and 7) to fit the adsorption data isothermally:[29,30]

$$q_e = \frac{Q_m K_L C_e}{1 + K_L C_e} \tag{6}$$

https://doi.org/10.1021/acsomega.4c00151
ACS Omega 2024, 9, 20142−20151

$$q_e = K_f C_e^{1/n} \quad (7)$$

where C_e is the lead ion concentration at adsorption equilibrium (mg/L), q_e and Q_m are the equilibrium adsorption capacity and saturated adsorption capacity (mg/g), respectively, and K_L and K_f are the isothermal adsorption equilibrium constants (L/mg). In the regeneration adsorption experiment, 0.5 M hydrochloric acid was used in a desorption−adsorption experiment on adsorbed SPI-PAA, and the test was performed five times.

3. RESULTS AND DISCUSSION

3.1. Stability of HIPEs. *3.1.1. Effects of SPI Concentration and Internal Phase Volume Fraction on the Stability of Pickering High Internal Phase Emulsions.* The emulsion prepared in the experiment was self-supporting, and there was no liquid flow even when the container was inverted (Figure 1). There was a certain accumulation of emulsion droplets on the surface as shown in the microscopy image, which is typical of a high internal phase emulsion. The HIPEs with an SPI concentration of 1.0% and different oil phase volumes are shown in Figure 2a−c. The HIPEs with an 80% stable internal phase at different SPI concentrations are shown in Figure 2d−f.

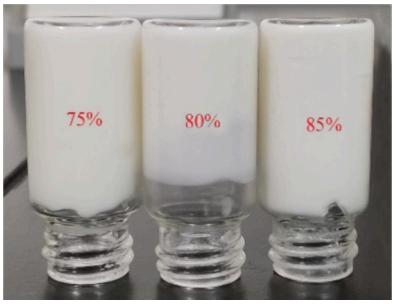

Figure 1. Emulsion appearance after inversion with different internal phase volume fractions.

When the oil phase volume was 75%, the particles stabilized the water−oil interface in an aggregated state. As the volume of the oil phase increased, the particles dispersed and changed from the initial aggregated state to a dispersed adsorption at the interface. As the oil phase increases, so does the actual particle concentration; therefore, the particle size is smaller when the oil phase is 80% than when it is 75%. When the oil phase was increased to 85%, the dispersed particles still continued to stabilize the interface, as the particle size of 85% was not significantly different from that of 80%.

When the protein concentration is low, there are insufficient particles adsorbed on the two-phase interface, resulting in an insufficient interface strength. Therefore, the probability of collisions between emulsion droplets increases, and they aggregate to form larger droplets. As the protein concentration increases, the number of particles participating in the formation of the interfacial film increases, creating film pressure and a barrier effect. These two events act together to reduce the particle size of the emulsion, which can then better maintain the structure of the emulsion droplets and improve the emulsion stability. There was no obvious difference in particle size between the 1.5 and 2.0% protein concentrations. It is possible that not all of the protein particles were adsorbed to the interface as the protein concentration increased; therefore, the emulsion particle size did not change significantly. However, as the protein concentration increased, the distance between emulsion droplets decreased, and the emulsion droplets were packed more tightly together.

3.1.2. Effect of Temperature on the Stability of Pickering High Internal Phase Emulsions. The results before and after heating of HIPEs with an SPI concentration of 1.0% and an internal phase volume fraction of 85% at 70 °C are shown in Figure 3. It can be seen that the appearance of the HIPEs did not change significantly and they still appeared to be in a solidified state. Under the microscope, we observed that the

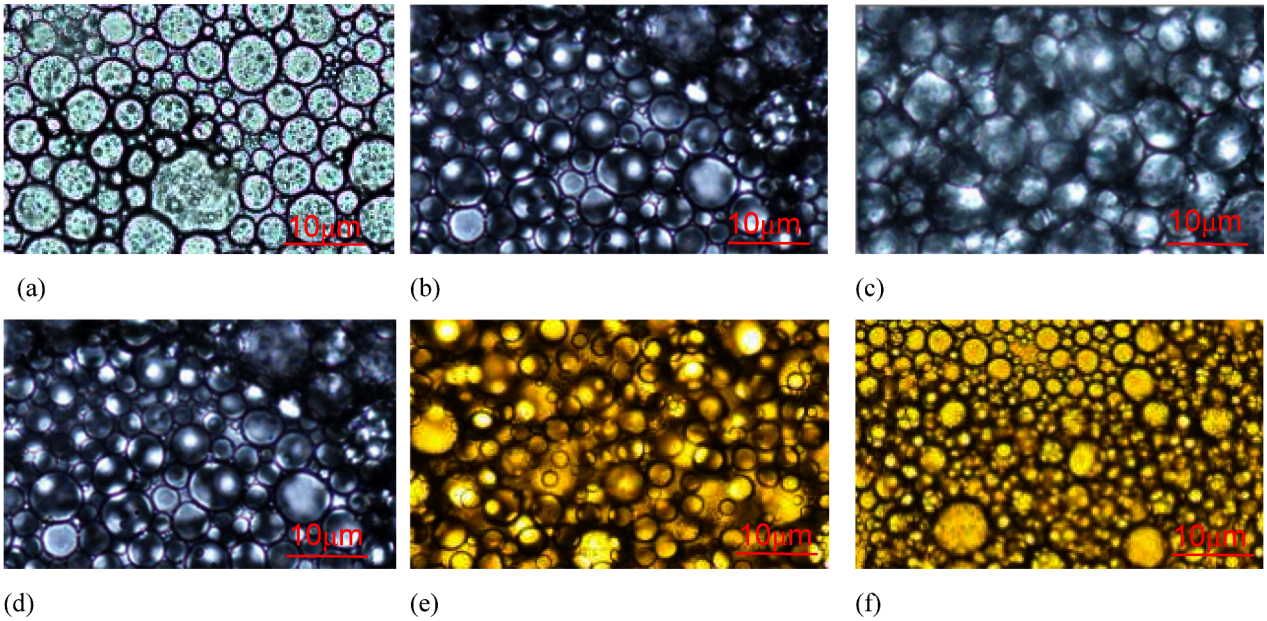

Figure 2. Microscopic images of a high internal phase emulsion with different internal phase volumes, (a) 75%, (b) 80%, and (c) 85%, and SPI concentrations, (d) 1.0%, (e) 1.5%, and (f) 2.0%.

https://doi.org/10.1021/acsomega.4c00151
ACS Omega 2024, 9, 20142−20151

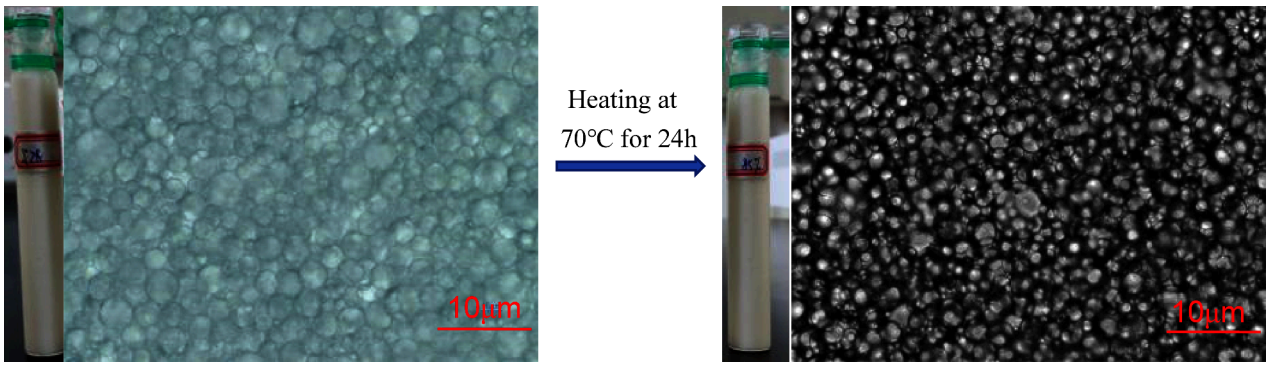

Figure 3. Microscopic appearance of high internal phase emulsion before and after heating at 70 °C for 24 h.

pore diameters tended to decrease, which allowed the particles to pack more tightly together. This may be due to the fact that high temperature causes the spatial structure of SPI to become disordered and its gelability to increase. At the same time, high temperature can expose noncovalent bonds or disulfide bond binding sites, which enhances the interaction between SPI and the oil−water interface, causing the gel network structure formed by it to become tighter. Thus, high-temperature stability is one of the characteristics of SPI-stabilized HIPEs, which is a beneficial property of HIPEs to be used as porous materials to prepare templates.

3.2. FT-IR Analysis. FT-IR was used to characterize the surface groups of SPI-PAA (Figure 4). The broad absorption

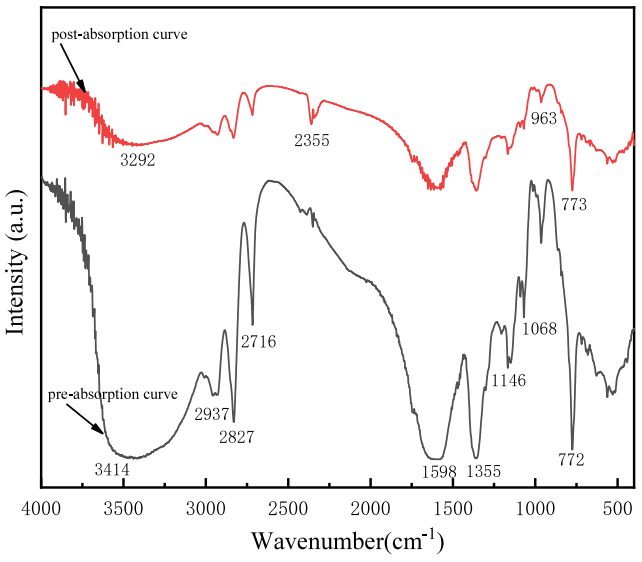

Figure 4. Infrared spectra of SPI-PAA before and after adsorption of lead ions.

peak at 3414 cm^{-1} corresponds to the superposition stretching vibration of −OH and $-NH_2$, indicating that there is a large amount of −OH and $-NH_2$ in SPI-PAA. The absorption peaks at 2937 and 2827 cm^{-1} are attributed to the stretching vibration absorption peaks of methyl and methylene, respectively. The absorption peak at 2716 cm^{-1} is attributed to the stretching vibration of −SH. The sharp peaks at 1598 and 1355 cm^{-1} respectively correspond to the stretching vibration absorption peak of −C═O and the bending vibration absorption peak of −OH. The peaks at 1146 and 1068 cm^{-1} are C−O stretching vibrations, and 963 cm^{-1} is H−O. Bending vibration indicates the presence of −COOH in SPI-PAA. The characteristic peak of $-NH_2$ is at 773 cm^{-1}.[31,32] The FT-IR characterization results show that there are active groups such as −COOH, $-NH_2$, −OH, and −SH in SPI-PAA. The percentages of functional groups are shown in Table 1.

Table 1. Relative Percentage of Functional Groups

functional group	relative percentage (%)
−COOH	31.47
$-NH_2$	7.05
−OH	13.00
−SH	1.45
−R	47.03

3.3. SEM Analysis of SPI-PAA Morphology. The appearance of SPI-PAA was observed under visible light, and the micromorphology was analyzed using a scanning electron microscope. The uniform thinness of the material allows light to easily pass through it (Figure 5, left panel). From the SEM

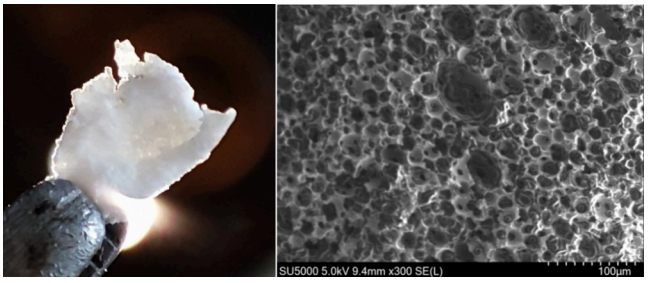

Figure 5. Light transmittance (left panel) and SEM image of porous SPI-PAA nanomaterial (right panel).

image, the pore structures inside SPI-PAA can clearly be seen (Figure 5, right panel). These pores are relatively uniformly distributed, and their average diameter is about 20 μm. Spatially, SPI-PAA presents a complex three-dimensional longitudinal structure with many pores and holes, which is consistent with Yu's research results.[25] This specialized morphological structure increases the contact area between SPI-PAA and other substances, which results in a greater adsorption capacity.

3.4. Specific Surface Area Analysis. The SPI-PAA nitrogen adsorption−desorption curve is type II, which is a typical physical adsorption−desorption curve for a mesoporous material (Figure 6). At lower pressures, the amount of nitrogen adsorbed was less, indicating that the composite had little or

https://doi.org/10.1021/acsomega.4c00151
ACS Omega 2024, 9, 20142−20151

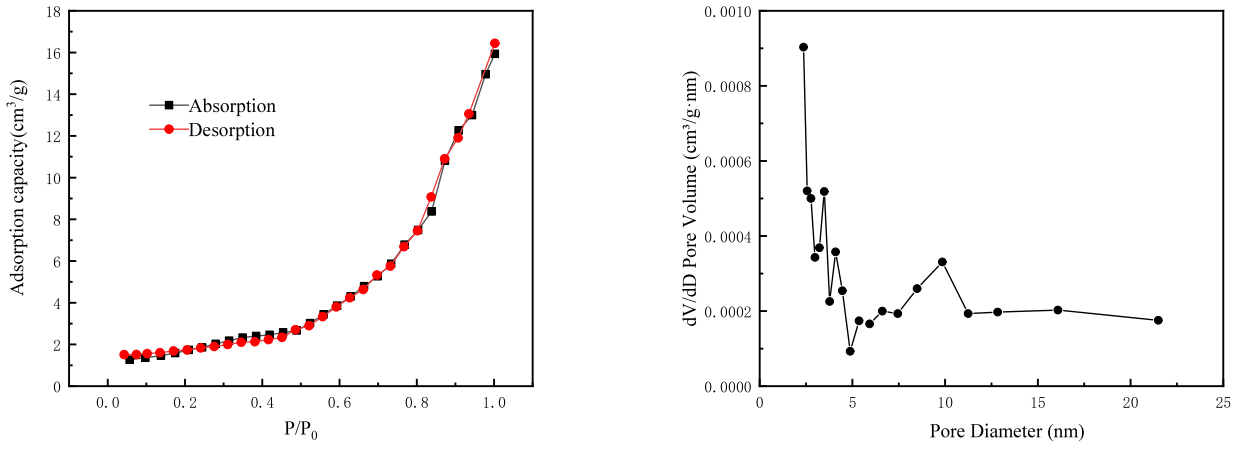

Figure 6. (a) N_2 adsorption−desorption curves of SPI-PAA; (b) pore size distribution of SPI-PAA.

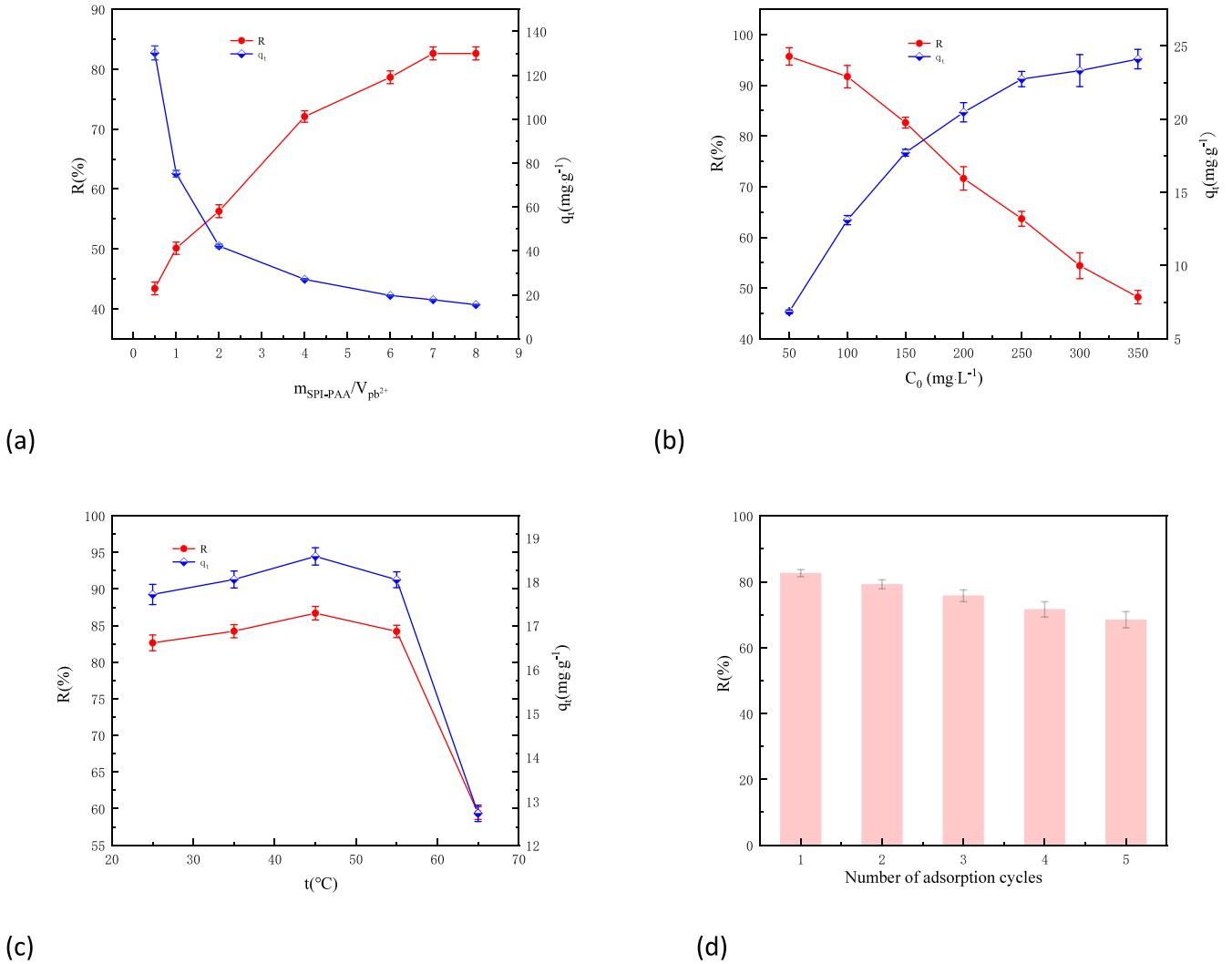

Figure 7. Effects of various factors on the SPI-PAA adsorption of Pb^{2+}. (a) Adsorbent dosage. (b) Initial concentration of Pb^{2+}. (c) Adsorption temperature. (d) Percent removal relative to desorption−adsorption rate of SPI-PAA.

no microporous structure. After single-layer adsorption was saturated, the pressure continued to increase and multilayer adsorption gradually occurred. At higher pressures, the amount of adsorbed gas increased rapidly, confirming the presence of an extensive macroporous structure in the material (surface area, 8.62 m^2/ g).

https://doi.org/10.1021/acsomega.4c00151
ACS Omega 2024, 9, 20142−20151

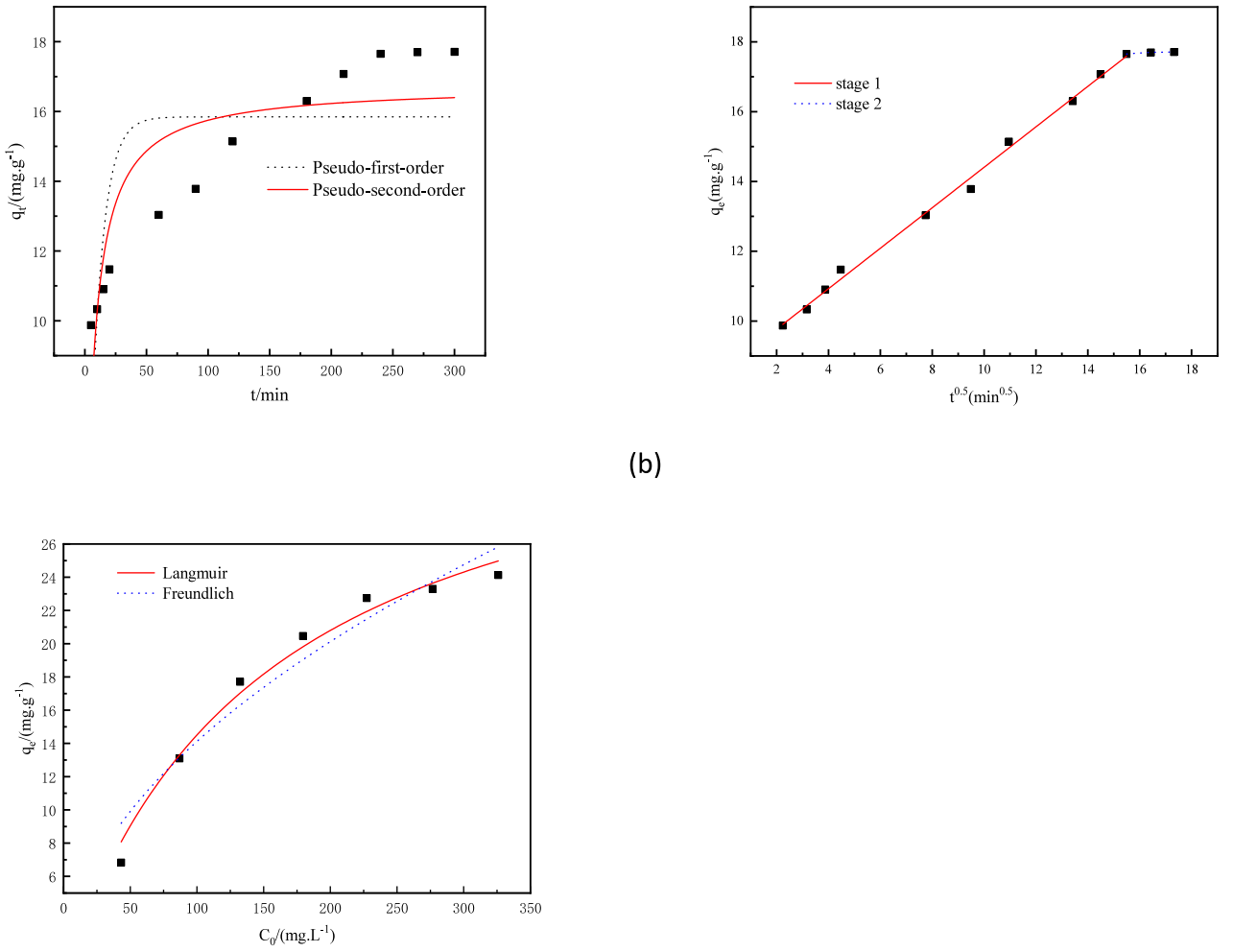

Figure 8. (a) Adsorption kinetics, (b) internal diffusion, and (c) isothermal adsorption of SPI-PAA.

3.5. Factors Affecting the Adsorption of Lead Ions by Composite Materials. *3.5.1. Effect of Adsorbent Dosage.* The effect of the adsorbent dosage on adsorption is shown in Figure 7a. As the amount of adsorbent increases, the removal rate of Pb^{2+} increases. When the adsorbent level is 4.0 g/L, the removal rate exceeds 72%. If the level continues to increase, then the removal rate also increases, albeit slowly. When the adsorbent reaches 7.0 g/L, the removal rate ceases to increase significantly. This is because the total number of active adsorption sites increases accordingly as the amount of adsorbent is increased, which, in turn, increases the removal rate of Pb^{2+}. However, due to limitations inherent in the adsorption equilibrium, when the amount of adsorbent is too high, the amount of adsorbed Pb^{2+} in the solution tends to plateau. This result is similar to that of Yang et al.[33] Meanwhile, as the amount of adsorbent is increased, the amount of Pb^{2+} adsorbed per unit mass decreases. To obtain the maximum Pb^{2+} adsorption rate, the concentration of the adsorbent has to be 7.0 g/L.

3.5.2. Effect of the Initial Concentration of Lead Ions. The effect of the Pb^{2+} concentration on SPI-PAA adsorption capacity is shown in Figure 7b. As the initial concentration of Pb^{2+} increases, the adsorption capacity of Pb^{2+} by SPI-PAA gradually increases, and the removal rate decreases. This is because the solute enters the active site of the solid adsorbent through diffusion, and the main driving force for diffusion is the concentration difference between the two phases. Increasing the concentration of metal ions can promote diffusion of Pb^{2+} into the inner layer of the adsorbent, which enhances the adsorption process. However, due to the limitations of the adsorbent itself, the removal rate decreases as the concentration of Pb^{2+} increases. When the initial concentration of Pb^{2+} is 200 mg/L, the removal rate is close to 72%, and when the initial concentration of Pb^{2+} is 50 mg/L, the removal rate is as high as 95.7%. This shows that SPI-PAA is more suitable for the removal of low concentrations of Pb^{2+} in water.

3.5.3. Effect of Adsorption Temperature. The effect of the adsorption temperature on SPI-PAA adsorption is shown in Figure 7c. As the adsorption temperature increases, the removal of Pb^{2+} by SPI-PAA first increases and then decreases. When the temperature is 45 °C, both the removal rate and adsorption capacity are at their highest values. This may occur because increasing the adsorption temperature under low temperature conditions can enhance the diffusion of the adsorbate, which increases the adsorption rate to a certain extent. However, when the temperature is too high, the reverse reaction rate increases because of the thermodynamics of

https://doi.org/10.1021/acsomega.4c00151
ACS Omega 2024, 9, 20142−20151

adsorption, which is not conducive to the forward progress of the adsorption reaction.

3.6. Adsorption Kinetics and Isothermal Adsorption. The adsorption kinetics and internal diffusion fitting curves of SPI-PAA are shown in Figure 8a,b, and the calculated adsorption kinetic parameters are shown in Table 2. The

Table 2. Kinetic Parameters of Pb^{2+} Adsorption

kinetics model	parameter	value
pseudo-first-order	$q_e/(mg{\cdot}g^{-1})$	16.59
	$k_1/(min^{-1})$	0.1022
	R^2	0.5265
pseudo-second-order	q_e /$(mg{\cdot}g^{-1})$	16.74
	$k_2/(g{\cdot}mg^{-1}{\cdot}min^{-1})$	0.0094
	R^2	0.7558

results show that adsorption increases with longer adsorption times and tends to reach equilibrium. The adsorption rate is relatively high in the first 30 min and approaches equilibrium around 240 min. The correlation coefficients of pseudo-first-order and second-order kinetic fitting are both low (first-order R^2 = 0.5265; second-order R^2 = 0.7558), and the theoretically calculated equilibrium adsorption capacity q_e is quite different from the experimentally obtained adsorption capacity q_t. This shows that the adsorption process does not follow either pseudo-first-order or second-order kinetics. The internal diffusion model was used to fit the entire adsorption process, and the linear correlation coefficient was low. If the fitting range is divided into two parts and the values corresponding to $t^{0.5}$ are 2−15 and 15−18, a good linear relationship can be obtained (2−15: R^2 = 0.9962; 15−18: R^2 = 0.9995), which shows that adsorption occurs in two stages. Some studies have shown that if the fitted straight line passes through the origin, it means that the adsorption rate is controlled by internal diffusion.[28] In this study, the regression line of the internal diffusion fitting did not pass through the origin, indicating that internal diffusion was not the only mechanism controlling the adsorption rate.

The isothermal adsorption of SPI-PAA is shown in Figure 8c, and the calculated isothermal adsorption parameters are shown in Table 3. The correlation coefficient fitted by the

Table 3. Isothermal Parameters of Pb^{2+} Adsorption

isotherm adsorption model	parameter	value
Freundlich	$1/n$	0.5108
	$K_f/(L{\cdot}mg^{-1})$	1.3443
	R^2	0.9293
Langmuir	$Q_m/(mg{\cdot}g^{-1})$	36.71
	$K_L/(L{\cdot}mg^{-1})$	0.0065
	R^2	0.9804

Langmuir isotherm model gives the best result, R^2 = 0.9804, indicating that the adsorption of Pb^{2+} by SPI-PAA conforms to the Langmuir isotherm model. It is generally believed that when $1/n$ is between 0.1 and 0.5, adsorption readily occurs, but when $1/n$ > 2.0, adsorption is slow.[30] Here, the value of $1/n$ was 0.5108, which is close to 0.5, indicating that the adsorption of Pb^{2+} by SPI-PAA was relatively easy to perform. According to the Langmuir isothermal adsorption fitting results, at saturation, the maximum adsorption capacity, Q_m, of SPI-PAA for Pb^{2+} was calculated to be 36.71 mg/g, which is higher than the Q_m of similar porous materials prepared by Yu using a high internal phase emulsion template method with wheat gliadin as a stabilizer (typical adsorption capacity of Pb^{2+} = 30.93 mg/g).[25]

3.7. Adsorbent Regeneration. SPI-PAA has a single removal rate of 82.64% for 150 mg/L lead ions (Figure 7d). As the number of regenerations increases, the removal effect gradually weakens, although after five repeated uses, the removal rate is still close to 70%. This shows that SPI-PAA has good reusability. Also, the desorption rate of lead ions after multiple regenerations of SPI-PAA is low, which may be related to the type of desorbent used and its concentration.

3.8. Adsorption Mechanisms. The kinetic and isothermal adsorption results show that internal diffusion is not the only mechanism of adsorption and that it also involves chemical effects. Combined with the results of FT-IR characterization of SPI-PAA, it can be seen that there are a large number of −COOH, $-NH_2$, −OH, −SH, and other active groups on the surface of SPI-PAA, which can complex with Pb^{2+} or coordinate such reactions (Figure 9). To clarify the adsorption

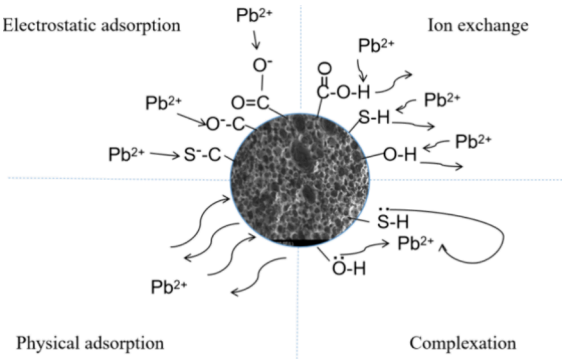

Figure 9. Mechanisms of the adsorption of lead ions by SPI-PAA.

mechanism, the molecular and structural changes before and after the SPI-PAA adsorption of Pb^{2+} were analyzed by FT-IR (Figure 3). Pb^{2+} adsorption by SPI-PAA generated a new strong absorption peak at 2355 cm^{-1} corresponding to the lead thiol complex, indicating that a complex or ion exchange reaction occurred between −SH and Pb^{2+}. At the same time, the −OH absorption peaks at 3470 and 963 cm^{-1} were significantly weakened, which is attributed to the coordination between the lone pair of electrons of hydroxyl oxygen and Pb^{2+}.[34,35] The above results showing the chemical interaction between SPI-PAA and Pb^{2+} confirm that the mechanism of Pb^{2+} adsorption by SPI-PAA includes physical effects such as pore filling and electrostatic attraction and chemical effects such as surface complexation and coordination, while the chemical effects of −COOH, −SH, and −OH on the surface of SPI-PAA are mainly adsorbance mechanisms.

An XPS energy spectrum analysis was also performed on SPI-PAA before and after the adsorption of Pb^{2+}, and the results are shown in Figure 10a. The XPS patterns of O 1s and S 2p before and after Pb^{2+} adsorption by SPI-PAA are shown in Figure 10b−d. After adsorbing Pb^{2+}, a Pb 4(f) absorption front appears at the SPI-PAA interface, indicating that SPI-PAA successfully adsorbs Pb^{2+} (Figure 10a). Before adsorption, C, O, and N on the SPI-PAA surface all have only one front in the XPS spectrum, and their binding energies are 284.77, 533.03, and 399.68 eV, respectively, indicating that before adsorption, all C, O, and N atoms on the SPI-PAA

https://doi.org/10.1021/acsomega.4c00151
ACS Omega 2024, 9, 20142−20151

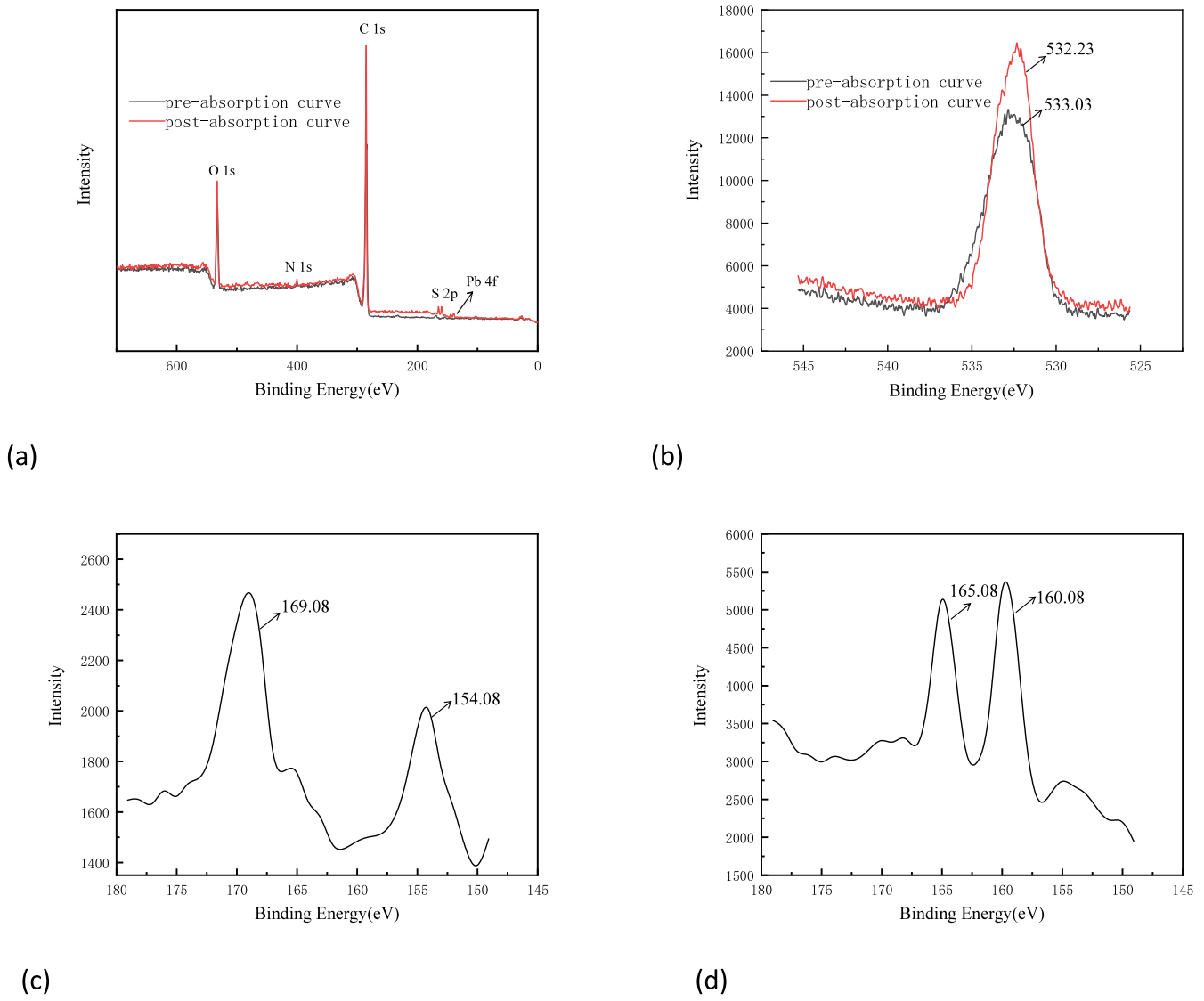

Figure 10. XPS spectra before and after Pb^{2+} adsorption by SPI-PAA. (a) Full picture; (b) O 1s; (c) before adsorption of S 2p; (d) after adsorption of S 2p.

interface are in the same chemical environment. The XPS spectrum of C 1s and N 1s electrons on the surface of the Pb^{2+}-SPI-PAA complex formed after adsorbing Pb^{2+} has only one peak, and its binding energies are still 284.77 and 399.68 eV, indicating that after adsorbing Pb^{2+} at the SPI-PAA interface, the chemical environment of C and N atoms does not change because the C and N atoms do not participate in coordination. However, the binding energy of O atoms shifted from 533.03 eV before adsorption to 532.23 eV (Figure 10b), indicating that the chemical environment of O atoms at the SPI-PAA interface has changed after adsorption of Pb^{2+}. According to the report in ref 36, we concluded that −COOH and −OH were involved in the coordination.[36] The binding energies of the absorption peaks of S 2p before adsorption are 154.08 and 169.08 eV, respectively (Figure 10c), which are considered to be formed by −SH and −C═S, respectively. The binding energies of the absorption peaks of S 2p after adsorption are 160.08 and 165.08 eV (Figure 10d); a large shift occurred, and the intensity became stronger. According to the evidence in refs 36 and 37, we concluded that −SH participated in the coordination.[36,37] The above results are consistent with the FT-IR analysis.

4. CONCLUSIONS

1. At an SPI mass fraction of 1.0%, a stable high internal phase acrylic emulsion with an internal phase volume fraction of 80% can be produced. Using this emulsion as a template, a macroporous polymer material with a three-dimensional interpenetrated pore structure can be synthesized by a polymerization reaction, with a specific surface area of 8.62 m^2/g. The surface of the material contains active groups such as −COOH, $-NH_2$, −OH, and −SH.
2. SPI-PAA is suitable for conditions with low initial metal concentration and low adsorption temperature and has good reusability. The maximum removal rate of Pb^{2+} in low-concentration solutions by SPI-PAA can reach 95.66%, and the maximum saturated adsorption capacity is 36.71 mg/g. The main mechanism of adsorption is chemical adsorption by active groups such as −COOH, −SH, and −OH.

https://doi.org/10.1021/acsomega.4c00151
ACS Omega 2024, 9, 20142−20151

3. Compared with previous high internal phase emulsion research, this study successfully replaced the use of small molecular weight surfactants and significantly reduced environmental pollution. The prepared SPI-PAA material has excellent adsorption capacity for Pb^{2+}.

■ ASSOCIATED CONTENT

Data Availability Statement

Data are contained within the article.

■ AUTHOR INFORMATION

Corresponding Author

Jierong Zhou − *Guilin University of Technology at Nanning, Nanning, Guangxi 530001, China*; Email: zhoujr@glut.edu.cn

Authors

Junzheng Wang − *Guilin University of Technology at Nanning, Nanning, Guangxi 530001, China*; orcid.org/0009-0008-0035-063X

Maofeng Zhu − *College of Chemistry and Bioengineering, Guilin University of Technology, Guilin, Guangxi 541006, China*

Complete contact information is available at: https://pubs.acs.org/10.1021/acsomega.4c00151

Author Contributions

Conceptualization: W.J.; investigation and validation: Z.M.; methodology and data curation: Z.J.; methodology, writing of the original draft, and editing: W.J.; project administration, review, and resources: W.J. and Z.J. All authors have read and agreed to the published version of the manuscript.

Funding

This research was funded by the National Natural Science Foundation of China (21964006) and Natural Science Foundation of Guangxi (2024GXNSFAA999150).

Notes

The authors declare no competing financial interest.

■ REFERENCES

(1) Kumari, S.; Agrawal, N. K.; Agarwal, A.; Kumar, A.; Malik, N.; Goyal, D.; Rajput, V. D.; Minkina, T.; Sharma, P.; Garg, M. C. prominent Streptomyces sp. biomass-based biosorption of zinc (II) and lead (II) from aqueous solutions: isotherm and kinetic. *Separations* **2023**, *7*, 393.

(2) Haris, M.; Shakeel, A.; Hussain, T.; Ahmad, G.; Ansari, M. S.; Khan, A. A. New trends in removing heavy metals from industrial wastewater through microbes. *Removal of emerging contaminants through microbial processes* **2021**, 183−205.

(3) Shrestha, R.; Ban, S.; Devkota, S.; Sharma, S.; Joshi, R.; Tiwari, A. P.; Kim, H. Y.; Joshi, M. K. Technological trends in heavy metals removal from industrial wastewater:A review. *J. Environ. Chem. Eng.* **2021**, *4*, No. 105688.

(4) Zhang, Y.; Yuan, K.; Magagnin, L.; Wu, X.; Jiang, Z.; Wang, W. Selective adsorption of Pb (II) and Cu (II) on mercapto-functionalized aerogels: Experiments, DFT studies and LCA analysis. *Journal of Cleaner Production* **2023**, *393*, No. 136126.

(5) Mahar, F. K.; He, L.; Wei, K.; Mehdi, M.; Zhu, M.; Gu, J.; Zhang, K.; Khatri, Z.; Kim, I. Rapid adsorption of lead ions using porous carbon nanofibers. *Chemosphere* **2019**, *225*, 360−367.

(6) Wang, J. Y.; Wang, L.; Zhang, W. L.; Wang, L.; Wei, Y.; Li, S. S.; Feng, J. T. Preparation of biochar-based composites and their adsorption performances for characteristic contaminants in wastewater. *Chem. Ind. Eng. Progress* **2019**, *08*, 3838−3851.

(7) Sobhani, M.; Tavakoli, H.; Chermahini, M. D.; Kazazi, M. Preparation of macro-mesoporous γ-alumina via biology gelatin assisted aqueous sol-gel process. *Ceram. Int.* **2019**, *1*, 1385−1391.

(8) Wang, Q.; Tang, P.; Ge, X.; Li, P.; Lv, C.; Wang, M.; Wang, K.; Fang, L.; Lu, X. Experimental and simulation studies of strontium/zinc-codoped hydroxyapatite porous scaffolds with excellent osteoinductivity and antibacterial activity. *Appl. Surf. Sci.* **2018**, *462*, 118−126.

(9) Yong, X.; Hu, Q.; Zhou, E.; Deng, J.; Wu, Y. Polylactide-based chiral porous monolithic materials prepared using the high internal phase emulsion template method for enantioselective release. *ACS Biomater. Sci. Eng.* **2019**, *10*, 5072−5081.

(10) Bago Rodriguez, A. M.; Binks, B. P. High internal phase Pickering emulsions. *Curr. Opin. Colloid Interface Sci.* **2022**, *57*, No. 101556.

(11) Bai, Y.; Pei, X.; Zhao, B.; Xu, K.; Zhai, K.; Wang, C.; Zhang, F.; Tan, Y.; Zhang, B.; Wang, Y.; Wang, P. Multiple pickering high internal phase emulsions stabilized by modified diatomite particles via one-step emulsification process. *Chem. Eng. Sci.* **2020**, *212*, No. 115341.

(12) Üzüm, G.; Akın Özmen, B.; Tekneci Akgül, E.; Yavuz, E. Emulsion-templated porous polymers for efficient dye removal. *ACS Omega* **2022**, *18*, 16127−16140.

(13) Yu, C.; Jiang, J.; Liu, Y.; Liu, K.; Situ, Z.; Tian, L.; Luo, W.; Hong, P.; Li, Y. Facile fabrication of compressible, magnetic and superhydrophobic poly (DVB-MMA) sponge for high-efficiency oil−water separation. *J. Mater. Sci.* **2021**, *56*, 3111−3126.

(14) Ou, H. x.; Gong, C. x.; Xue, H. l.; Zhou, D. s.; Li, K. j.; Liu, S. c. Adsorption of tetrodotoxin by flexible shape-memory polymers synthesized from silica-stabilized Pickering high internal phase emulsion. *Adsorption* **2021**, *10*, 805−818.

(15) Zhou, X.; Liu, E.; Li, J.; Chen, F.; Zhang, Y.; Chen, K.; Qi, D. Facile Synthesis of Rodlike TiO_2/Lignin Nanostructures as Multifunctional Emulsifiers for High Internal Phase Emulsions. *ACS Appl. Nano Mater.* **2023**, *16*, 14820−14830.

(16) Kang, Z.; Hu, H.; Uyama, H.; Zhang, B. x. Porous Eucommia ulmoides Gum Monoliths Prepared via Modified Pickering High Internal Phase Emulsion Method. *ACS Appl. Polym. Mater.* **2023**, *8*, 6117−6123.

(17) Recio-Colmenares, C. L.; Ortíz-Rios, D.; Pelayo-Vázquez, J. B.; Moreno-Medrano, E. D.; Arratia-Quijada, J.; Torres-Lubian, J. R.; Huerta-Marcial, S. T.; Mota-Morales, J. D.; Pérez-García, M. G. Polystyrene Macroporous Magnetic Nanocomposites Synthesized through Deep Eutectic Solvent-in-Oil High Internal Phase Emulsions and Fe_3O_4 Nanoparticles for Oil Sorption. *ACS Omega* **2022**, *25*, 21763−21774.

(18) Jiao, B.; Shi, A.; Wang, Q.; Binks, B. P. High-internal-phase Pickering emulsions stabilized solely by peanut-protein-isolate microgel particles with multiple potential applications. *Angew. Chem., Int. Ed.* **2018**, *30*, 9274−9278.

(19) Dai, L.; Yang, S.; Wei, Y.; Sun, C.; McClements, D. J.; Mao, L.; Gao, Y. Development of stable high internal phase emulsions by Pickering stabilization:Utilization of zein-propylene glycol alginate-rhamnolipid complex particles as colloidal emulsifiers. *Food Chem.* **2019**, *275*, 246−254.

(20) Zhou, F. Z.; Yu, X. H.; Zeng, T.; Yin, S. W.; Tang, C. H.; Yang, X. Q. Fabrication and characterization of novel water insoluble protein porous materials derived from Pickering high internal-phase emulsions stabilized by gliadin-chitosan-complex particles. *J. Agric. Food Chem.* **2019**, *12*, 3423−3431.

(21) Wang, C. Z.; Guan, X.; Sang, J.; Zhou, J. J.; Wang, C. H.; Ngai, T.; Lin, W. General liquid vegetable oil structuring via high internal phase Pickering emulsion stabilized by soy protein isolate nanoparticles. *Journal of Food Engineering.* **2023**, *356*, No. 111595.

(22) Wang, Z.; Zhao, Y. B.; Liu, H. T.; Chen, Q.; Liu, Q.; Kong, B. H. Soy protein isolate-sodium alginate colloidal particles for improving the stability of high internal phase Pickering emulsions. *Effects of mass ratios.Food Chemistry: X* **2024**, *21*, No. 101094.

(23) Xu, X. Y.; Li, L.; Ma, C. M.; Li, D.; Yang, Y.; Bian, X.; Fan, J.; Zhang, N.; Zuo, F. Soy protein isolate-citrus pectin-gallic acid ternary composite high internal phase Pickering emulsion for delivery of β-carotene: Physicochemical, structural and digestive properties. *Food Research International* **2023**, *169*, No. 112910.
(24) Rehman, A.; Liang, Q.; Karim, A.; Assadpour, E.; Jafari, S. M.; Rasheed, H. A.; Virk, M. S.; Qayyum, A.; Rasul Suleria, H. A.; Ren, X. Pickering high internal phase emulsions stabilized by biopolymeric particles: From production to high-performance applications. *Food Hydrocolloids* **2024**, *150*, No. 109751.
(25) Yu, Y. Y. *Development and Application of Protein-Based Porous Materials via Pickering High Internal Phase Emulsion Templates*; South China University of Technology: Guangzhou,2019.
(26) Ma, L.; Zou, L.; McClements, D. J.; Liu, W. One-step preparation of high internal phase emulsions using natural edible Pickering stabilizers: Gliadin nanoparticles/gum Arabic. *Food Hydrocolloids* **2020**, *100*, No. 105381.
(27) Torrik, E.; Soleimani, M.; Ravanchi, M. T. Application of kinetic models for heavy metal adsorption in the single and multicomponent adsorption system. *International Journal of Environmental Research* **2019**, *13*, 813−828.
(28) Lemma, L.; Kiflie, Z.; Kassahun, S. K. Adsorption of Pb^{2+} and Cd^{2+} on the l-cysteine-functionalized graphene oxide/chitosan/polyvinyl alcohol hydrogel: Kinetic, isotherm, and thermodynamic study. *Rem. J.* **2023**, *3*, 233−248.
(29) Hu, L.; Zheng, J.; Li, Q.; Tao, S.; Zheng, X.; Zhang, X.; Liu, Y.; Lin, X. Adsorption of 5-hydroxymethylfurfural, levulinic acid, formic acid, and glucose using polymeric resins modified with different functional groups. *ACS Omega* **2021**, *26*, 16955−16968.
(30) Yuan, M.; Liu, D. S.; Liu, W.; Song, Z. H.; Shang, S. S.; Wang, Z. H.; Ren, J.; Cui, S. Graphene oxide/polydopamine modified montmorillonite/carboxymethyl chitosan composite aerogel for efficient removal of Pb^{2+}, Cu^{2+}, and Cd^{2+}: Adsorption behavior, mechanism and DFT study. *Sep. Purif. Technol.* **2024**, No. 126585, DOI: 10.1016/j.seppur.2024.126585.
(31) Wang, Z.; Zhang, G.; Li, Y. Preparation of chitosan/polyacrylamide/graphene oxide composite membranes and study of their methylene blue adsorption properties. *Materials* **2020**, *19*, 4407.
(32) Lu, T.; Zhu, Y.; Wang, W.; Qi, Y.; Wang, A. Interconnected superporous adsorbent prepared via yeast-based Pickering HIPEs for high-efficiency adsorption of Rb^{+}, Cs^{+} and Sr^{2+}. *Chemical Engineering Journal* **2019**, *361*, 1411−1422.
(33) Yang, X. W.; Li, Z. G.; Li, P. Z.; Wang, J. T. Preparation of sodium alginate gel sponge and its adsorption for Pb^{2+} and Cu^{2+}. *Fine Chem.* **2021**, *1*, 162−168.
(34) Shi, T.; Xie, Z.; Mo, X.; Feng, Y.; Peng, T.; Song, D. Highly efficient adsorption of heavy metals and cationic dyes by smart functionalized sodium alginate hydrogels. *Gels* **2022**, *6*, 343−13.
(35) Zou, Y. Cu^{2+}, Cd^{2+}, and Pb^{2+} ions adsorption from wastewater using polysaccharide hydrogels made of oxidized carboxymethyl cellulose and chitosan grafted with catechol groups. *Iran. Polym. J.* **2024**, *1*, 57−66.
(36) Yang, Y. R.; Zeng, L.; Lin, Z. K.; Jiang, H. B.; Zhang, A. P. Adsorption of Pb^{2+}, Cu^{2+} and Cd^{2+} by sulfhydryl modified chitosan beads. *Carbohydr. Polym.* **2021**, *274*, No. 118622.
(37) Guo, N.; Liao, B.; Lu, T.; Liu, S. L. Simultaneous Removal of Cadmium and Congo Red from Wastewater Using Modified Chitosan. *Hydrometall. China* **2023**, *5*, 503−511.

https://doi.org/10.1021/acsomega.4c00151
ACS Omega 2024, 9, 20142−20151